Segregation, precipitation, and α-α' phase separation in Fe-Cr alloys

A. Kuronen
Department of Physics, University of Helsinki, P.O. Box 43, FI-00014 Helsinki, Finland

S. Granroth, M. H. Heinonen, R. E. Perälä, T. Kilpi, P. Laukkanen, J. Lång, J. Dahl, M. P. J. Punkkinen, and K. Kokko*
Department of Physics and Astronomy, University of Turku, FI-20014 Turku, Finland
and Turku University Centre for Materials and Surfaces (MatSurf), Turku, Finland

M. Ropo
Department of Physics, Tampere University of Technology, P.O. Box 692, FI-33101 Tampere, Finland
and COMP, Department of Applied Physics, Aalto University, Finland

B. Johansson
Applied Materials Physics, Department of Materials Science and Engineering, Royal Institute of Technology, SE-10044 Stockholm, Sweden
and Department of Physics and Materials Science, Uppsala University, SE-75121 Uppsala, Sweden

L. Vitos
Applied Materials Physics, Department of Materials Science and Engineering, Royal Institute of Technology, SE-10044 Stockholm, Sweden;
Department of Physics and Materials Science, Uppsala University, Box 516, SE-75120 Uppsala, Sweden;
and Research Institute for Solid State Physics and Optics, Wigner Research Center for Physics, P.O. Box 49, H-1525 Budapest, Hungary

(Received 28 April 2015; revised manuscript received 7 December 2015; published 28 December 2015)

Iron-chromium alloys, the base components of various stainless steel grades, have numerous technologically and scientifically interesting properties. However, these features are not yet sufficiently understood to allow their full exploitation in technological applications. In this work, we investigate segregation, precipitation, and phase separation in Fe-Cr systems analyzing the physical mechanisms behind the observed phenomena. To get a comprehensive picture of Fe-Cr alloys as a function of composition, temperature, and time the present investigation combines Monte Carlo simulations using semiempirical interatomic potential, first-principles total energy calculations, and experimental spectroscopy. In order to obtain a general picture of the relation of the atomic interactions and properties of Fe-Cr alloys in bulk, surface, and interface regions several complementary methods have to be used. Using the exact muffin-tin orbitals method with the coherent potential approximation (CPA-EMTO) the effective chemical potential as a function of Cr content (0–15 at. % Cr) is calculated for a surface, second atomic layer, and bulk. At ∼10 at. % Cr in the alloy the reversal of the driving force of a Cr atom to occupy either bulk or surface sites is obtained. The Cr-containing surfaces are expected when the Cr content exceeds ∼10 at. %. The second atomic layer forms about a 0.3 eV barrier for the migration of Cr atoms between the bulk and surface atomic layer. To get information on Fe-Cr in larger scales we use semiempirical methods. However, for Cr concentration regions less than 10 at. %, the *ab initio* (CPA-EMTO) result of the important role of the second atomic layer to the surface is not reproducible from the large-scale Monte Carlo molecular dynamics (MCMD) simulation. On the other hand, for the nominal concentration of Cr larger than 10 at. % the MCMD simulations show the precipitation of Cr into isolated pockets in bulk Fe-Cr and the existence of the upper limit of the solubility of Cr into Fe layers in Fe/Cr layer systems. For high Cr concentration alloys the performed spectroscopic measurements support the MCMD simulations. Hard x-ray photoelectron spectroscopy and Auger electron spectroscopy investigations were carried out to explore Cr segregation and precipitation in the Fe/Cr double layer and $Fe_{0.95}Cr_{0.05}$ and $Fe_{0.85}Cr_{0.15}$ alloys. Initial oxidation of Fe-Cr was investigated experimentally at 10^{-8} Torr pressure of the spectrometers showing intense Cr_2O_3 signal. Cr segregation and the formation of Cr-rich precipitates were traced by analyzing the experimental atomic concentrations and chemical shifts with respect to annealing time, Cr content, and kinetic energy of the exited electron.

DOI: 10.1103/PhysRevB.92.214113 PACS number(s): 68.35.bd, 68.35.Dv, 68.47.De, 71.15.Nc

I. INTRODUCTION

Iron-chromium alloys have many technologically important and scientifically interesting properties [1]. On the other hand, growing technological challenges are faced in designing multifunctional steels. Developing of advanced steels to meet different standards simultaneously, e.g., high strength, proper workability and ductility, excellent corrosion resistivity, and specific magnetic properties, all in various ambient conditions, requires breakthrough innovations and cutting edge research [2]. Iron and chromium are typical examples of a ferromagnet and an antiferromagnet, respectively. As a function of composition and structure the magnetic properties of Fe-Cr vary considerably; e.g., spin glass [3] and giant magnetoresistance [4] features are found in these systems.

*kalevi.kokko@utu.fi

The crystallographic properties of Fe-Cr are also peculiar. Although Fe-Cr has a body-centered-cubic (bcc) based structure within the whole composition range, there exist both stable and metastable composition regions in the phase diagram. The experimental phase diagram of Fe-Cr at 300 °C shows the miscibility gap beginning from 5–10 at. % and extending to 90–95 at. % Cr. Within this miscibility gap two domains exist, regions of spinodal decomposition and nucleation and growth. The latter is located at the outskirts of the miscibility gap extending about 20 at. % on each side [5]. Upon aging Fe-Cr often undergoes transformation to either a high-temperature σ phase or separation into Fe-rich (α) and Cr-rich (α') phases [6–9]. In 20 at. % Cr alloy at 773 K temperature after 50 h annealing precipitates have been observed to occupy 2% of the alloy volume [8]. The microscale changes in the crystallographic properties may induce considerable changes at macroscopic level; e.g., the "475 °C embrittlement" [10,11] has significant effect on the mechanical properties of certain steel grades. Fe-Cr is the base component in many stainless steel grades due to the beneficial properties of chromium. A certain amount of chromium makes an iron alloy corrosion resistant [12]. At ambient conditions a thin and transparent film of chromium oxide rapidly forms on the open surface of the alloy preventing further oxidation and blocking corrosion. The corrosion resistance of the ferritic stainless steels increases abruptly by several orders of magnitude when the Cr content in the bulk reaches ∼10 at. % level [13]. This oxidation-related experimental threshold of Cr content in the bulk coincides with the calculated reversal point of the relative magnitudes of the Fe and Cr chemical potentials in the bulk and surface of the Fe-Cr alloys. This reversal of the relative chemical potentials enables the outburst of Cr on the otherwise pure Fe surface found exclusively in the case of low-Cr Fe-Cr alloys [14]. Therefore, at ambient conditions Cr_2O_3 is easily formed on the surface of $Fe_{1-x}Cr_x$ ($x \gtrsim 0.1$) alloys. Furthermore, due to the strong tendency of Cr to segregate to the Fe-Cr/Cr_2O_3 interface [15], there is an additional driving force for a Cr_2O_3 layer to grow until the surface oxide reaches the protective nanometer scale thickness preventing the further oxidation of the material. Due to their technological importance and challenging open questions, such as how to form a complete picture of the Cr segregation to the surface and the formation of the protective Cr oxide scale, the surfaces of Fe-Cr alloys have recently received considerable scientific attention [12,14,16–21].

In this work, we investigate the physical conditions and possible realizations of segregation, precipitation, and phase separation in Fe-Cr systems. Our objectives are (i) to extend the concentration-dependent *ab initio* investigations of the driving force of Cr diffusion to the subsurface atomic layer, (ii) to use a semiempirical method to extend the above investigation to a larger spatial scale, (iii) to improve the theoretical understanding of the surface segregation of Fe-Cr alloys by combining the results of (i) and (ii), (iv) to investigate spectroscopically the Cr segregation in the Fe/Cr double layer and Fe-Cr alloys by using thermal treatments of samples of different compositions, (v) to use very low oxygen pressure to investigate the initial stage of the protective surface oxide scale, and (vi) to assess the validity of the computational results by comparison with the experiments. To get a comprehensive picture of the state of Fe-Cr as a function of composition, temperature, and time the present investigation combines Monte Carlo simulations using semiempirical interatomic potential, *ab initio* total energy calculations, and experimental spectroscopy. Using several complementary methods it is possible to get a more reliable picture of the interactions between Fe and Cr atoms and explain the consequences of the atomic interactions for the properties of Fe-Cr alloys. *Ab initio* methods are used to get the atomic-scale energetics as a function of the concentration of the alloys, the thermodynamics of large-scale systems is obtained with the Monte Carlo method, and experimental spectroscopy is used to probe the concentrations and atomic structure of real Fe-Cr systems as a function of Cr content and annealing time. However, one should carefully take into account the scope of validity of each method. Keeping this in mind our aim is to give an extensive picture of the atomic structure in bulk, surface, and interface regions in Fe-Cr systems. The rest of the paper is divided into two main sections and conclusions. The research methods are briefly reviewed in Sec. II and the results are presented and discussed in Sec. III.

II. METHODS

A. First-principles calculations

The *ab initio* total energy calculations are based on the density functional theory [22,23] and were performed using the exact muffin-tin orbitals (EMTO) method [24,25]. The basis set includes s, p, d, and f orbitals. The generalized gradient approximation in the PBE form was used for the exchange-correlation functional [26]. The total energy was calculated using the full charge-density technique [25,27]. The alloys were simulated as a substitutionally disordered bcc ferrite phase using the coherent potential approximation (CPA) which provides the continuous scanning of the concentration of the alloy [28]. There are two magnetic degrees of freedom in the calculations: the magnetic moments of iron and chromium atoms. The absolute value and sign of these moments are determined by optimizing the total energy of the alloy. The calculated equilibrium lattice constant was used for each composition. The EMTO approach in combination with the CPA has been applied successfully in the theoretical study of various structural and electronic properties of alloys and compounds [25] demonstrating the level of accuracy and efficiency needed also in the present investigation. For more details of the electronic structure calculations we refer to our earlier work [14,29].

The basic quantities used in the present study are surface energy (E_{surf}), segregation energy (E_{segr}), chemical potential (μ), and mixing enthalpy per atom (E_{mix}). The effective chemical potential ($\Delta\mu^{\mathrm{b}}$) and the slope of the mixing enthalpy of bulk Fe-Cr are related within a simple relation [30],

$$\Delta\mu^{\mathrm{b}} = (\mu_{\mathrm{Fe}} - \mu_{\mathrm{Cr}})^{\mathrm{bulk}} \approx -\frac{\partial E_{\mathrm{mix}}}{\partial x} + \text{constant}, \qquad (1)$$

where x is the atomic fraction of Cr [$N_{\mathrm{Cr}}/(N_{\mathrm{Fe}} + N_{\mathrm{Cr}})$; N_{Fe} and N_{Cr} are the number of Fe and Cr atoms in the investigated system, respectively]. The surface energy is defined as the energy needed to form a new surface per the formed new surface area:

$$E_{\mathrm{surf}} = \frac{E_{\mathrm{slab}} - E_{\mathrm{bulk}}}{2A}, \qquad (2)$$

where E_{slab} is the energy of the slab system with two surfaces, both having the area A. E_{bulk} is the energy of the bulk system having the same amount of atoms as the slab system. The segregation energy of Cr from a region A to a region B is defined as the energy needed to transfer a Cr atom from A to B and an Fe atom from B to A:

$$E_{\text{segr}}^{\text{Cr:A}\rightarrow\text{B}} = \Delta\mu^{\text{A}} - \Delta\mu^{\text{B}}. \quad (3)$$

Our choice for the present mean-field CPA approximation is motivated by the fact that alternative methods such as the cluster expansion approximation or the supercell approach would increase the computational load enormously without adding substantial new physics to the present problem. We notice that both the bulk enthalpy of formation and the surface segregation phenomena in Fe-Cr have been discussed using some of these alternative methods [19,29,31,32], and a comparison with the EMTO-CPA predictions demonstrates the validity of our approach.

B. Large-scale Monte Carlo simulations

Because *ab initio* simulations for large systems and for longer time scales are not possible we performed Monte Carlo simulations for $Fe_{1-x}Cr_x$ alloys to test the *ab initio* predictions and to investigate the *thermodynamic ground state* of the alloys in larger scales.

Due to the time-consuming simulations and large systems, *ab initio* methods cannot be used. Thus the interatomic interaction was modeled by a semiempirical potential, namely the two-band embedded atom model (2BEAM) which is designed to reproduce the mixing enthalpy of the Fe-Cr alloy [33]. One should note that the 2BEAM potential is optimized mainly for bulk properties.

Precipitation and segregation of chromium in finite temperatures and in large systems was studied using the Monte Carlo (MC) method where possible moves included atom displacements and exchange of types (Fe or Cr) of a pair of atoms. Displacements were performed with short sequences of molecular dynamics (MD) simulations in the canonical ensemble. Using MD was observed to be more efficient in moving atoms than the conventional Metropolis algorithm with atomic displacements. All Monte Carlo–molecular dynamics (MCMD) simulations were performed in the *NVT* ensemble with the proper value of the lattice constant obtained from separate *NPT* simulations as a function of temperature and chromium concentration. It should be emphasized that the MCMD calculations are pure equilibrium simulations; there is no kinetics involved. Equilibrium simulations were chosen instead of kinetic modeling due to the fact that having polycrystalline targets in the experiments may imply fast diffusion paths on grain boundaries. Modeling grain boundary diffusion near surfaces using the kinetic Monte Carlo method is a considerable effort and is left for future work. We believe, however, that the equilibrium simulations do give insight into the phase separation in FeCr alloys.

The MCMD method was used to study the near-surface structure of the Fe-Cr alloy and the structure of an iron-chromium interface in a layered system. In the simulations a system of size $86 \times 86 \times 86$ Å^3 with 54 000 atoms was used. The lengths of the simulations varied from 80 000 to 120 000 MC steps and results were calculated by taking the averages of roughly 40 000 last simulation steps. For the surface studies boundary conditions were applied in the x and y directions while leaving the two (001) z surfaces open. In the case of layer structure simulations periodic boundary conditions were applied in all three directions. The interface orientation was (001).

Surface structure simulations were performed in temperatures of 300, 500, and 700 K and interface simulations in 300 and 700 K.

The Fe-Cr system has been studied previously using the MC method and different models for interaction. In rigid lattice MC simulations [12,20,34–37] using Ising-type interaction the Hamiltonian must be made temperature dependent. Semiempirical potentials have been used in both Metropolis MC (MMC) [38–40] and kinetic MC (KMC) [9,41–47] studies. All works on kinetics are bulk simulations of single-crystal alloys and diffusion mediated by a single vacancy.

In the MMC work by Zhurkin *et al.* [40] the 2BEAM potential by Olsson *et al.* [48] (a similar model but with slightly different parametrization) was used to study Cr segregation at surfaces and on dislocations. However, the authors presented results only for chromium concentrations of 5% and 10% and did not calculate the chromium segregation energy as a function of nominal chromium concentration (see Fig. 4).

Another work addressing free surfaces is the one by Levesque [12] where the MMC method was used with a DFT-based Ising-type Hamiltonian. The model used by the author is based on a rigid lattice. Consequently, the vibrational part of the entropy must be included as an explicit temperature dependence of the Hamiltonian. Thus, the model is very different from the MCMD/2BEAM used in this work where vibrational degrees of freedom are included by definition. On the other hand, both these models are based on bulk properties of the iron-chromium alloys.

C. Experiments

The Fe/Cr bilayer was grown by electron beam physical vapor deposition from elemental Fe and Cr on a Si substrate. The top Fe layer of the Fe/Cr/Si sandwich was grown to about 50 nm thickness to protect the sample from contamination and mechanical failure. The thickness of the Fe film was checked by sputtering. The Fe-Cr alloy samples were prepared by induction melting under argon flow from elemental components. The Cr bulk concentrations are 5 and 15 at. % for samples $Fe_{0.95}Cr_{0.05}$ and $Fe_{0.85}Cr_{0.15}$, respectively. The concentrations 5 and 15 at. % Cr were selected to encompass the interesting concentration region of the onset of the corrosion resistance (9–13 at. % Cr) in ferritic stainless steels and the *ab initio* prediction of the onset of the surface segregation of Cr in Fe-Cr alloys (8–9 at. % Cr) [14]. Elemental components of purity better than 99.99% were used for all the samples. To start the investigations with fresh and unoxidized samples sputtering and annealing were used to remove all contamination. The Fe layers of Fe/Cr/Si were cleaned in the UHV of the analyzer chamber of the spectrometer by annealing at 150 °C followed by 20 min argon sputtering. To clean the alloy samples Ar sputtering was carried out until no traces of oxygen or carbon were detected. The atomic diffusion was driven by varying

the temperature of the samples. The bilayer sample and alloys were heated to 500 °C at rate 30 °C/min for different times and then cooled close to room temperature.

The photoemission spectra were collected using both conventional x-ray photoelectron spectroscopy (XPS) (PHI ESCA 5400 Electron Spectrometer, Perkin Elmer) with non-monochromatic Al Kα radiation at a home laboratory and synchrotron-radiation-excited hard x-ray photoelectron spectroscopy (HAXPES) with a high kinetic energy (HIKE) experimental station [49] at the KMC-1 beamline at Helmholtz-Zentrum Berlin (HZB), Bessy II. The VG Scienta R4000 electron analyzer, modified for electron kinetic energies up to 10 keV, and a high-resolution double-crystal monochromator were used. To obtain photon energies from 2300 to 7300 eV, Si(111), Si(311), and Si(422) crystals of the monochromator were selected for the presented measurements. The x-ray incidence angle was approximately 4° in every experiment and the photoelectrons were detected in normal emission. The energy scale was calibrated using Fermi level of the samples and the Au $4f$ spectra of the calibration sample. The adjustable photon energy range from about 2 keV to 10 keV makes it possible to study photoelectrons with high kinetic energy which increases their inelastic mean-free path (IMFP) making the HAXPES technique bulk sensitive as a comparison to surface-sensitive laboratory XPS or soft x-ray range synchrotron radiation. Thus bulk-sensitive investigations of atomic concentrations and chemical state of compound elements are possible without altering the original sample structure or chemistry by sputtering. Also depth-profiling can be done by measuring core levels with different binding energies and thus photoelectrons with different IMFPs or by exploiting different sampling depths of specific core electrons by adjusting the photon energy of radiation. The high photon energy range makes it possible to measure photoelectrons with very high binding energy (low kinetic energy), for example Cr or Fe 1s at 5990 and 7110 eV, which enables also surface-sensitive studies to be performed using HAXPES.

In addition we have used conventional Auger electron spectroscopy (AES) with the Physical Electronics Model Cylindrical Mirror Analyzer to carry out depth profiling through the whole Fe/Cr bilayer before and after heating until the Si substrate is reached. The depth profiles of the samples were obtained using Ar^+ sputtering (3000 V, 4×4 mm^2 area, about 8 mPa Ar^+ pressure and 2 μA sample current). After every 1 minute sputtering cycle O KLL, Cr LMM, and Fe LMM spectra from 400 to 760 eV were measured. The O and Cr spectra are overlapping and to get reliable quantitative information we used reference spectra of Fe, Cr, and O (AlO) measured using the same equipment and parameters. The AES profiles were obtained from differentiated spectra of Fe/Cr bilayers and reference samples after background subtraction using factor analysis delivered by principal component analysis (PCA) of CasaXPS 2.13.16 (Fig. 10).

III. RESULTS AND DISCUSSION

We begin the structural analysis of Fe-Cr alloys by using the *ab initio* data to formulate some basic atomic models of the surface segregation and bulk precipitation of Cr. The next step is to perform MC simulations for larger systems to obtain results for more realistic cases. Finally, we use photoelectron spectroscopy to experimentally determine the segregation and precipitation in the Fe/Cr double layer and Fe-Cr alloys as a function of annealing time and concentration.

TABLE I. Calculated (EMTO) bulk mixing enthalpy (E_{mix}) and the bulk to surface (surface layer: s_1, second layer: s_2) segregation energy of Cr ($E_{\mathrm{segr}}^{\mathrm{Cr:b}\to s_1,s_2}$) of homogeneous Fe-Cr as a function of atomic % of Cr in the bulk (c_{b}). $c_{\mathrm{b}} = 3$ at. % corresponds to the minimum of E_{mix}. Negative (positive) mixing enthalpy means stable (metastable) bulk phase; negative (positive) $E_{\mathrm{segr}}^{\mathrm{Cr:b}\to s}$ means a driving force to a Cr-containing (pure-Fe) surface. The two upper rows are calculated using an 8 atomic layer slab in our previous work [14] and the two lower rows are the present results of 12 atomic layer calculations.

c_{b} (at. %)	0	3	5	10	12	15	20	25
E_{mix} (meV)	0	−2.8	−1.8	10.2		27.7	44.3	60.0
$E_{\mathrm{segr}}^{\mathrm{Cr:b}\to s_1}$ (meV)	251			−59		−16	60	
$E_{\mathrm{segr}}^{\mathrm{Cr:b}\to s_1}$ (meV)	216	204	145	−47	−71	−58		
$E_{\mathrm{segr}}^{\mathrm{Cr:b}\to s_2}$ (meV)	314	358	364	248	213	204		

A. Initial relaxation in the surface region

Magnetic effects have been shown to be the origin of segregation, precipitation, and phase separation in Fe-Cr alloys [50–56]. The magnetic moments of iron atoms tend to align parallel whereas the magnetic moments of chromium atoms tend to align antiparallel. In low-Cr Fe-Cr alloys chromium moments align antiparallel to the iron moments to reduce the energy of the alloy. However, in Cr-rich Fe-Cr alloys the antiparallel coupling of the Cr moments with the Fe matrix inevitably leads to parallel coupling between the moments of the chromium atoms leading to an increase in energy with increasing Cr content. The effects of the magnetic configuration on the total energy of the Fe-Cr alloy and the atomic magnetic moments in the four topmost atomic layers and in the bulk have been calculated and discussed in our previous investigation [29]. It has been shown that this kind of magnetic frustration has a key role in the miscibility of the Fe-Cr alloys [17].

Besides on external conditions, the structural evolution of an initially homogeneous Fe-Cr alloy depends crucially on the concentration of the alloy and the relative magnitudes of the atomic diffusion rates at different spatial regions of the alloy. Using the *ab initio* data shown in Table I and in Fig. 1 we can make predictions for the structural evolution of initially homogeneous $Fe_{1-x}Cr_x$ alloys (same concentration throughout the whole bulk and surface regions). Since atomic diffusion rates are usually significantly higher in the near-surface regions than in the bulk [57] it is natural to split the consideration into initial surface relaxation and more retarded bulk relaxation. For nonhomogeneous alloys, the structural evolution depends also on the gradients of the Cr concentration.

We begin our analysis by considering the relaxation of the near-surface region connected to the bulk reservoir with fixed concentration. According to the *ab initio* segregation energy ($E_{\mathrm{segr}}^{\mathrm{Cr:s_2}\to s_1} = \Delta\mu^{s_2} - \Delta\mu^{s_1}$, where s_1 and s_2 refer to

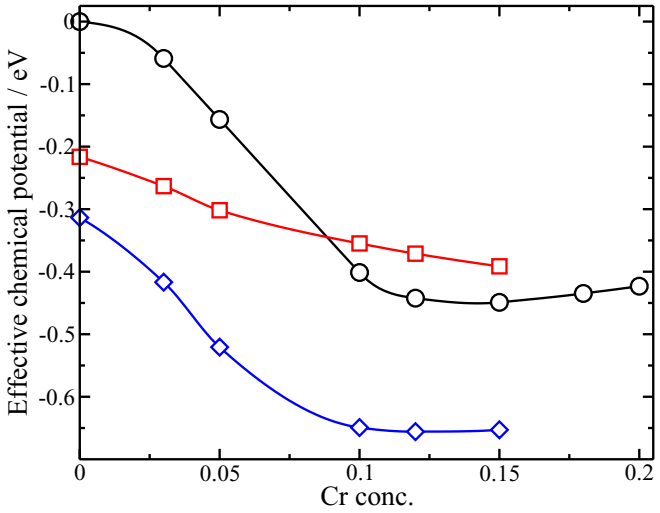

FIG. 1. (Color online) Calculated (EMTO) effective chemical potential $\Delta\mu = \mu_{\mathrm{Fe}} - \mu_{\mathrm{Cr}}$ of the surface atomic layer (red squares), second atomic layer (blue diamonds), and bulk (black circles) as a function of Cr content of the homogeneous alloy. The open symbols are calculated points; the curves are guides to the eye. In the present calculations we have used larger unit cells, 12 atomic (100) layers separated by vacuum of thickness equivalent to 6 atomic layers, compared to the previous work [14], where 8 atomic layers of metal slab were separated by vacuum of thickness equivalent to 4 atomic layers.

the surface and second atomic layer, respectively; Fig. 1), the initial driving force ($E_{\mathrm{segr}}^{\mathrm{Cr:s_2\to s_1}} < 0$) within the two surface atomic layers pushes Cr atoms from the second layer to the surface layer. This driving force is increased by a factor of 3, from ~98 meV to ~295 meV, when the Cr concentration of the alloy increases from 0 at. % to 10 at. %. As Fig. 1 shows, the driving force on Cr atoms between the bulk and the surface atomic layer is for low Cr alloys from the surface to the bulk, but when the Cr concentration exceeds ~10 at. % this driving force turns in the opposite direction pushing Cr atoms from the bulk to the surface. For all investigated alloy concentrations the second atomic layer forms a diffusion barrier for a Cr atom to move from the bulk to the surface atomic layer. The barrier starts from ~310 meV at 0 at. % Cr and decreases to ~250 meV at 10 at. % Cr. This can be compared with other *ab initio* calculations [21] using a 36 atom supercell including one Cr impurity atom and giving a 355 meV barrier for the second atomic layer. From Fig. 3 we see also that the model consisting of homogeneous bulk and two surface atomic layers describes the energetics of Fe-Cr (100) surfaces quite well because the segregation energy is practically converged to the bulk value at the third atomic layer.

To sum up, our *ab initio* calculations predict a Cr-depleted surface atomic layer for Fe-Cr alloys below 10 at. % Cr, a stable Cr-enriched surface atomic layer within the bulk Cr content between 10 and 18 at. % (a typical situation in many commercial steel grades), and a Cr-containing stable surface beyond 18 at. % Cr. The second atomic layer is predicted to be depleted in Cr. Since $E_{\mathrm{segr}}^{\mathrm{Cr:b,s_2\to s_1}}$ increases with increasing Cr surface concentration, there exists a concentration-dependent upper limit for the Cr content at the surface, as posed by the condition $E_{\mathrm{segr}}^{\mathrm{Cr:b,s_2\to s_1}} = 0$ [14].

B. Bulk-surface relaxation

Considering the thermodynamic ground state of the whole bulk-surface Fe-Cr system, the bulk part should be relaxed too. The mixing enthalpy of $Fe_{1-x}Cr_x$ (Table I) suggests that if the Cr concentration of the alloy exceeds ~10 at. %, the bulk part of the alloy has a tendency to transform to an α-α' phase-separated system: Cr-rich precipitates immersed in the $Fe_{0.97}Cr_{0.03}$ alloy. The Cr-rich α' precipitates are expected to avoid the contact with the surface because the surface energy of Cr is higher than that of Fe. Therefore, a low-Cr zone under the surface is expected to be formed driving the initially formed Cr-containing surface back to the pure Fe surface. However, this can happen only in vacuum. In ambient conditions the surface is expected to oxidize rapidly. Because the Cr affinity to oxygen is much higher than that of Fe, Cr_2O_3 islands are expected to be formed on the surface. Due to the driving force of Cr to enrich the metal/Cr_2O_3 interface [15] these islands can grow until the uniform protective oxide layer is formed on the surface. Therefore, Cr at the surface is bound to an oxide form, and the surface of Fe-Cr is practically in an inert state during the retarded α-α' phase separation in the bulk.

C. Monte Carlo simulations

The predictions of the basic properties of Fe-Cr systems by the potential model are shown in Figs. 2, 3, and 4, where the surface and segregation energies are shown. The energies of the (100) and (110) surfaces calculated by the 2BEAM are considerably lower when compared with the *ab initio* results. However, the differences between the energies of iron and chromium are similar when comparing the 2BEAM and *ab initio* results. Furthermore, all calculated energies differ from the experimental values, which are also scattered and based partly on semiempirical estimates.

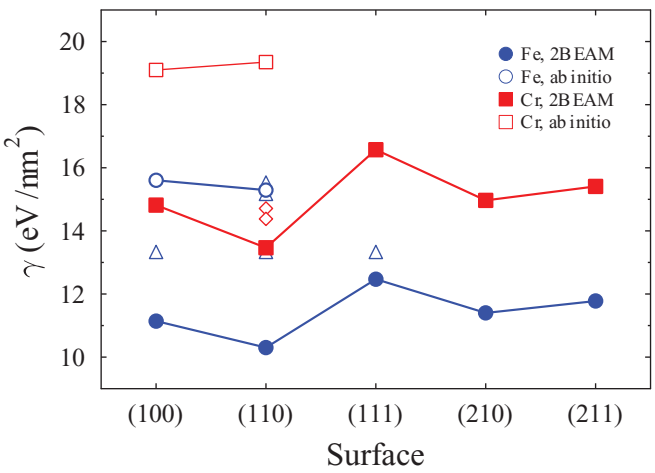

FIG. 2. (Color online) Surface energies of low-index surfaces of bcc iron and chromium as predicted by the 2BEAM model. Results of *ab initio* calculations (open circles for Fe and open squares for Cr) are from Ref. [58]. Experimental values (open triangles for Fe and open diamonds for Cr) are from Ref. [60].

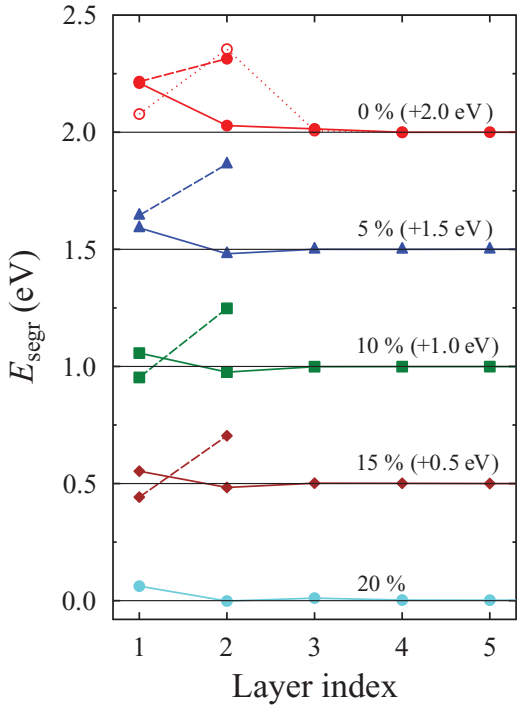

FIG. 3. (Color online) Segregation energy of a chromium atom in iron chromium alloy in the near-surface atomic layers for different chromium concentrations as predicted by the 2BEAM model (solid lines) and *ab initio* (dashed lines) calculations (Table I). Curves are shifted by the marked amount for better visibility. The *ab initio* result for the pure iron from Ref. [21] is plotted with dotted line and open symbols.

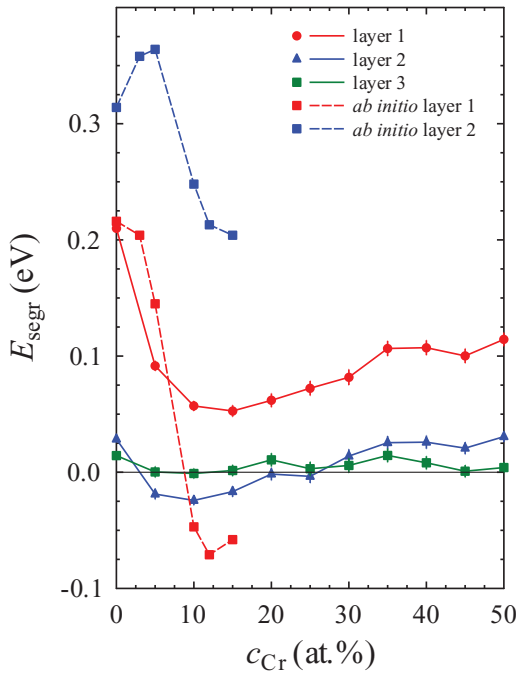

FIG. 4. (Color online) Segregation energy of the three near-surface atomic layers as a function of bulk Cr concentration as predicted by the 2BEAM model. The *ab initio* data are the ones presented in Table I.

Surface segregation energies for different alloy concentrations were calculated as averages of 1000 random alloy samples. Segregation energy was defined as the energy difference between configurations where the Cr atom was in the center of the simulation box and when the atom was in one of the near-surface atomic layers. One should note that the variation of the segregation energy in different samples was large (in the range 0.1–0.2 eV) compared to the energy itself. The error bars (barely visible) in Figs. 3 and 4 are the errors of the mean. The figures show that there is a barrier for chromium atoms to segregate to the alloy surface. However, for alloys of chromium concentrations in the range of 5–20 at. % the segregation energy to the second atomic layer is negative predicting Cr segregation to the second layer. Comparing the 2BEAM results with the *ab initio* data of Levesque *et al.* [21] at the Cr impurity level the 2BEAM model predicts larger (smaller) segregation energy for the surface layer (second layer). On the other hand, the EMTO segregation energy (Table I) is close to the 2BEAM value for the surface layer but close to the result of Levesque *et al.* [21] for the second layer. Figure 4 shows essentially the same data as Fig. 3 but plotted along the Cr concentration axis. Here the *ab initio* data are from Table I. As Fig. 4 shows the EMTO results predict Cr segregation to the surface when Cr concentration exceeds 10 at. %, whereas the MCMD results predict that the segregation of Cr to the surface is prevented by an energy barrier but Cr segregation is expected to the second atomic layer within the range of 5–20 at. % Cr concentration. One should also note that there is a discrepancy between the two *ab initio* results for the surface layer of pure iron: 0.078 eV (Ref. [21]) vs 0.216 eV (Table I). One notices from Figs. 3 and 4 that for the segregation energy E_{segr} the *ab initio* methods predict stronger oscillations as a function of layer position or the concentration than the MCMD method. This can be partly related to the difference of model systems used in the calculations. In the *ab initio* calculations there is only one type of surroundings for a Cr atom in a specific layer whereas in MCMD calculations, in principle, every Cr atom has a different surrounding. Therefore the MCMD results are "averaged" which possibly leads to reduced oscillations in E_{segr}.

The difference between the results obtained by various computational approaches is expected to be mainly due to the specific approximations and implementations of the computational methods. The EMTO results were obtained relaxing the volume of the alloy uniformly (without local atomic relaxations) and random occupation of atomic sites was simulated using the CPA; i.e., the model system in our case is a homogeneous alloy. Levesque *et al.* [21] used the supercell approximation with fully relaxed atomic coordinates to model an impurity Cr atom. Their model system consisted of one Cr atom in the unit cell. The average overall bulk concentration in their calculations corresponds to a few at. % Cr and the planar concentration of Cr impurity is 25 at. % for a ($2a \times 2a \times 4a$) slab (a being the lattice constant). For layer relaxations of pure Fe they reported -0.02 Å for the surface layer and 0.04 Å for the second layer. A recent investigation based on the same *ab initio* method [58,59] found -0.002 Å for the surface and 0.04 Å for the second-layer relaxations. This indicates that although there is a good agreement for the subsurface layer the top layer results are very different in

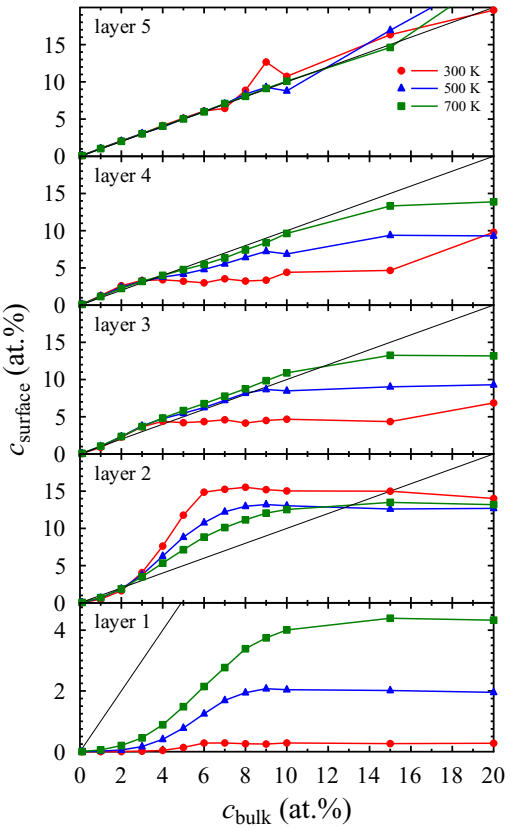

FIG. 5. (Color online) Chromium concentration of near-surface atomic layers as a function of the average bulk concentration. Gray lines show the one-to-one relation between the bulk and layer concentrations. Note the different y axis scale in the case of layer 1.

these two pseudopotential *ab initio* investigations. Here we report similar behavior for the segregation energies too. The differences between the results of Punkkinen *et al.* [58,59] and Levesque *et al.* [21] could be partly due to the smaller slab and vacuum thicknesses and the using of constant-volume atomic relaxation in the latter investigation. The semiempirical potentials in the MCMD method are optimized mainly for bulk properties, which somewhat limits its feasibility for surface studies.

Since the accurate modeling of the surfaces and large bulk systems of Fe-Cr alloys at different temperatures is beyond the reach of any single computational technique we are forced to use several theoretical approaches to get the comprehensive overall picture. The results of Levesque *et al.* [21] are considered to describe the impurity in bulk, but due to the relatively small cell size these data cannot account for the impurity effects on the surface. Considering surface regions at higher Cr concentrations the EMTO method is expected to perform better and for large bulk systems, as a function of temperature, the MCMD is the natural choice.

Figure 5 shows the near-surface concentrations from the surface layer (layer 1) up to the fifth atomic layer (layer 5) as a function of bulk chromium concentration c_{bulk}. At 300 K the surface layer is exclusively occupied by Fe atoms up to ~5 at. % Cr in the bulk. At that point the Cr concentration at the surface jumps slightly upwards (to ~0.3 at. %). With increasing temperature the qualitative shape of the concentration curve of layer 1 does not change appreciably, but the height of the jump gets larger, however, staying considerably lower than the average Cr concentration in the bulk (thin gray line in Fig. 5). The MCMD result for the bulk concentration threshold of the Cr-containing surfaces (c_{bulk} ~ 5–6 at. %) compares reasonably well with the *ab initio* results (8–9 at. %) [14]. However, the *ab initio* investigations predict the concentration of Cr at the surface to exceed the bulk value whereas in MCMD simulations the Cr concentration at the surface stays below the bulk value. This is related to the fact that the 2BEAM model predicts a strongly positive segregation energy for a Cr atom in the surface layer.

The plateau beyond ~10 at. % Cr in the bulk seen in the concentration curves of layer 1 suggests that the Cr content in nearby atomic layers has reached a certain saturation value. This is what actually happens as can be seen in the panel of layer 2: the Cr content saturates to the ~13 at. % value at the bulk concentration of c_{bulk} ~ 8 at. %. With increasing depth from the surface the layer-resolved concentration curves gradually approach the average bulk concentration line, as expected. However, one should remember that the profiles shown in Fig. 5 are averaged concentrations parallel to the surface plane direction. The bulk part of Fe-Cr is expected to be α-α' phase separated at higher bulk concentrations, where the thermodynamically optimal state consists of Cr-rich precipitates (c_{Cr} = 80–90 at. %) in a homogeneous Fe-Cr alloy containing a few percent of Cr. Since the surface energy of Fe-Cr is in this model minimized by an Fe surface, the probability of finding a Cr-rich precipitation in the near-surface region is low. This is also clearly seen in Fig. 5. The Cr concentrations of the third and fourth layers level off to values below the average bulk value when the Cr content in bulk is above the α-α' phase separation threshold (average Cr content in bulk 6, 10, and 15 at. % for the 300, 500, and 700 K simulations, respectively). In the case of layer 2 the increase of the concentration above the average bulk value at c_{bulk} = 3%–13% can also be attributed to the negative segregation energy of a Cr atom in the second layer at these bulk concentrations.

One should note that the Ising-type model presented in Ref. [35] and used to model FeCr surfaces in Ref. [12] also predicts chromium depletion from the surface (in this case two topmost layers instead of one as in this work). Similar compensatory increase of chromium concentration in the layer below the depleted layer(s) is then observed: in layer 3 in the case of Ref. [12] and layer 2 in the current work.

In Fig. 6 the cross sections of the MCMD simulation box are shown for concentrations c_b = 5, 10, 15, and 20 at. % at simulation temperatures 300 K and 700 K. The low probability of Cr-rich α' precipitates touching the surface is clearly demonstrated. Adding Cr increases the number and size of Cr-rich precipitates leaving the rest of the alloy in a homogeneous low-Cr state in agreement with recent theoretical and experimental investigations [7–9]. Figure 7 shows the concentration profiles corresponding to the MCMD simulations shown in Fig. 6. One can see that when the bulk concentration c_{bulk} is below ~10 at. % the surface depth profile of the Cr concentration shows only the short-period screening

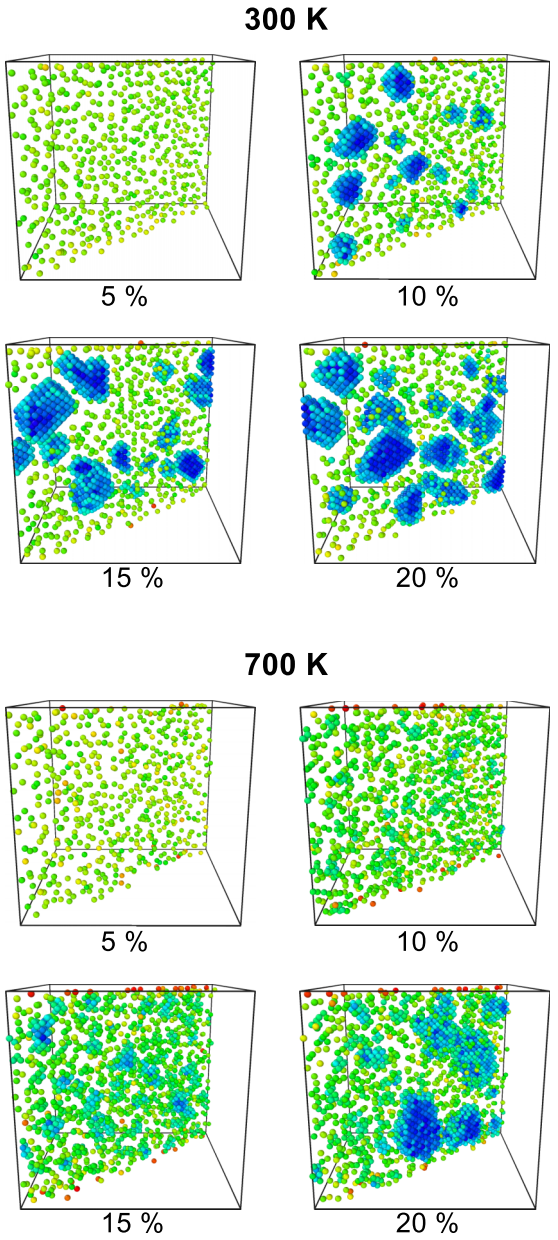

FIG. 6. (Color online) Snapshots of the simulated $Fe_{1-x}Cr_x$ systems at different temperatures and with different chromium concentrations x. Figure shows slices of thickness 15 Å in the (110) direction. Only chromium atoms are shown with color coding according to potential energy (blue color representing low potential energy). The top and bottom facets of the simulation box are open surfaces.

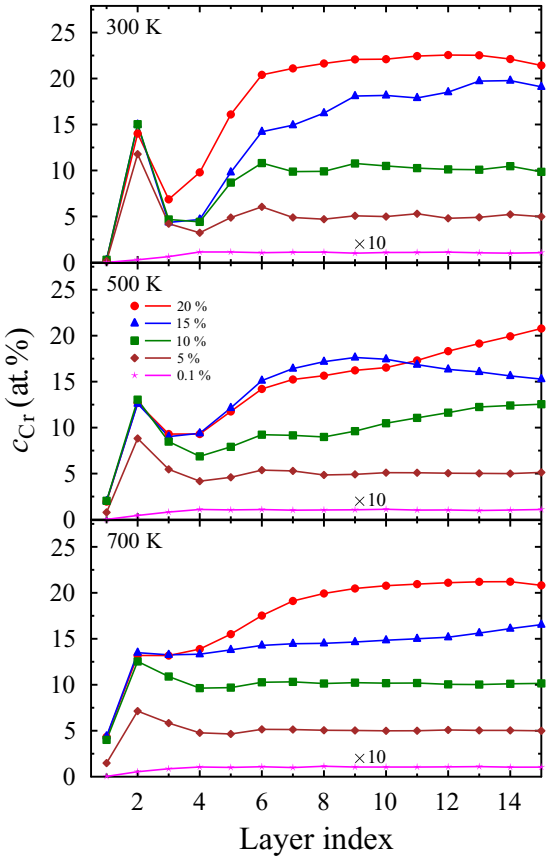

FIG. 7. (Color online) Chromium concentration depth profiles for different average chromium concentrations and simulation temperatures. Curves for 0.1% are multiplied by 10 for better visibility.

effect due to the surface perturbation leveling off to the bulk concentration in deeper layers. These oscillations are similar as observed in the MMC simulation of the (111) surface by Zhurkin *et al.* [40]. For concentrations $c_{\mathrm{bulk}} \gtrsim 10$ at. % long-period oscillations due to the Cr-rich precipitates show up deeper in the sample. An almost fixed ∼13 at. % Cr value in the second atomic layer is observed due to the interactions of Cr-rich precipitates and the surface in line with the *ab initio* predictions.

Figure 8 shows depth profiles similar to those of Fig. 7 but with the Cr precipitates removed. This was done by discarding all the atoms that had the average atomic type index larger than 1.5 where 1.0 corresponds to pure Fe and 2.0 to pure Cr. We see that in the bulk part the concentration reaches the solubility limit of the Cr in Fe (6, 10, and 15 at. % for the 300, 500, and 700 K simulations, respectively). Concentrations of the surface layers are essentially the same as in Fig. 7 because the chromium precipitates do not extend to the surface layers. With the effect of the precipitates removed, Fig. 8 also shows clearly the range and the decay rate of the concentration fluctuations due to the screening of the surface perturbation. The low Cr content in the first layer is overcompensated by layer 2, which is back-compensated by layers 3 and 4, etc. As expected, the compensation amplitude decreases with increasing distance from the surface and the concentration fluctuations are less pronounced at higher temperatures.

Considering the experimental investigations of segregation and precipitation in Fe-Cr it would be beneficial to study, in addition to alloys, also Fe/Cr layer structure. In the layer structure one can study the evolution of Fe-Cr as a function of Cr concentration in a more transparent way because the density gradient is a one-dimensional function. Similarly in this case the segregation of Cr in the surface of the Fe layer can also be investigated in a controlled way. With these benefits in mind, we finish our simulations by considering the Fe/Cr layer structure. Figure 9 shows the results of the simulations of the Fe/Cr interface. The dashed curves are the initial states in

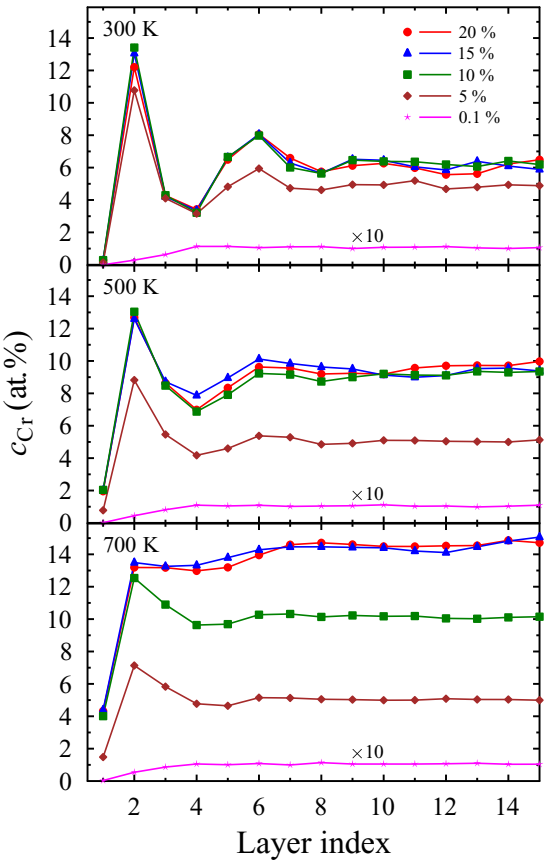

FIG. 8. (Color online) As in Fig. 7 but with chromium precipitates removed. Removing was done by discarding atoms whose average type during the last 60 000 simulation steps was larger than 1.5 where the value 1.0 corresponds to pure Fe and 2.0 to pure Cr.

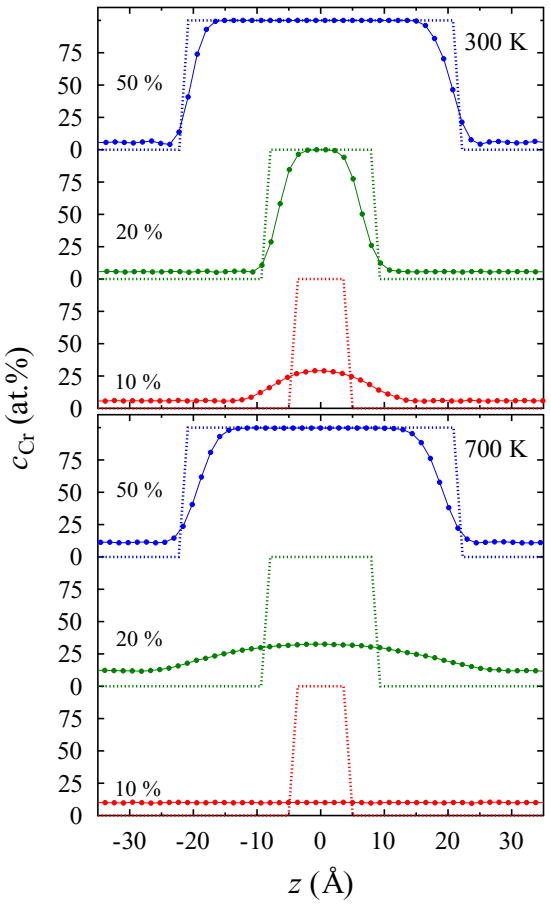

FIG. 9. (Color online) Cr concentration profiles for the layer widths corresponding to different total Cr concentrations simulated in different temperatures. Thin dashed lines show the initial Cr profile.

which there exist pure Cr and Fe sections in the simulation cell, whereas the solid lines show the situation after the simulation. The results show that the thermodynamical ground state of the investigated system consists of two different parts: low Cr section where the average Cr concentration is ∼6 at. % at 300 K (∼12 at. % at 700 K, which compares well with experimental results of about 14 at. % at 773 K [8]) and the excess of the Cr remains in the original Cr part. In the case of temperature of 700 K and original concentration of 10 at. % the whole Cr layer is dissolved into the Fe. This is expected as the solubility of Cr in Fe at this temperature is over 10 at. %. At the lower temperature of 300 K the original layer is partly dissolved leaving precipitates with mainly (110) facets. Also, for the 700 K case with 20 at. % chromium the layer structure changes into a single precipitate again with (110) facets. The appearance of (110) facets is in line with *ab initio* interface calculations [61] which show that the (110) interface has the lowest energy which compares well with the surface energies in Fig. 2. The 300 K, 50 at. % case shows oscillations of the concentration profile which are caused by a similar compensation effect to that on the surface and partly by the faceting of the interface. These oscillations are washed out when the temperature is raised to 700 K and the positions of the atoms become more random.

D. Segregation, precipitation, and oxidation in Fe-Cr systems

1. Verification of the theoretical predictions

Our theoretical predictions in a nutshell are as follows: (i) According to the *ab initio* calculations in low Cr alloys ($\lesssim$ 10 at. %) the two topmost surface atomic layers are depleted from Cr whereas in Cr-rich alloys Cr segregation to the surface atomic layer is predicted. (ii) Semiempirical simulations predict that in Cr-rich alloys separate Cr-precipitated regions are formed, and these Cr-rich α' dumplings are spread into a homogeneous α phase alloy containing 6 at. % (12 at. %) chromium at 300 K (700 K). Considering the Fe/Cr double layer the Cr layer donates Cr atoms to the Fe layer until a temperature-dependent critical Cr content in the Fe layer has been reached. The obtained theoretical predictions are compared with the experimental results as follows: (1) Nondestructive depth profiling using different photon energies in HAXPES enables us to estimate the relative concentrations as a function of the probing depth. (2) Analyzing the core level shifts gives us information on the surroundings of the target atom that can be related to the oxidized Cr, Cr segregation, or Cr precipitation. (3) AES provides a tool to investigate, using different heat treatments, the Cr concentration profile of the Fe/Cr double layer. In the following, experimental work and results are discussed in more detail.

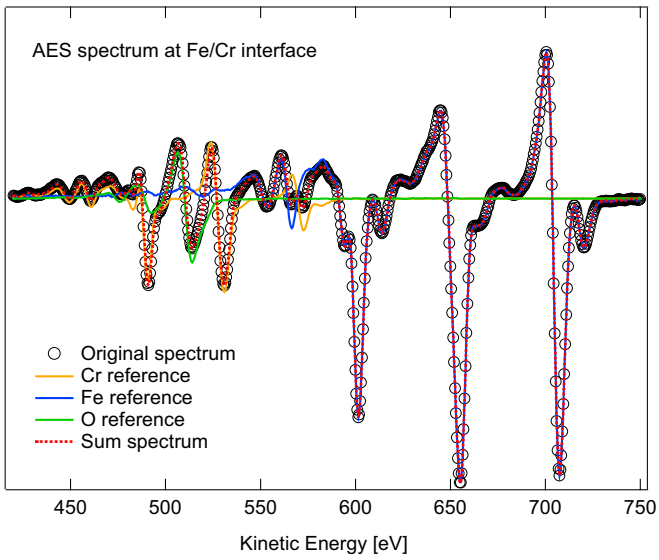

FIG. 10. (Color online) Example of an AES spectrum of Fe/Cr interface ("o" curve) of Fe/Cr/Si sample. The sum spectrum (dashed curve) was obtained by principal component analysis (PCA) of CasaXPS 2.13.16 [63].

2. *Cr segregation in Fe/Cr bilayer and Fe-Cr alloys*

Experimentally the segregation of Cr can be demonstrated by comparing the concentrations of Cr and Fe atoms as a function of the probing depth. We have used two different methods to carry out depth profiling for Fe/Cr/Si samples. In AES the topmost atoms are removed by ion gun layer by layer and after every sputtering cycle the Cr and Fe Auger electron spectra (Fig. 10) are collected and the intensities of the compound elements are compared. However, due to ion bombardment sputtering is considered as a destructive method and it may have unwanted effects on some concentration values. For example, preferential sputtering or reduction of oxides can be a drawback in some studies. Preferential sputtering is not a problem in case of Fe and Cr but the analysis of the oxide layer can be. This technique is not ideal for chemical analysis which is why HAXPES spectra measured using different photon energies (different IMFP of photoelectrons) was important to collect as well. Due to the limited time for synchrotron radiation experiments it is impossible to measure HAXPES spectra layer by layer but the use of three selected photon energies and analysis of different core-level spectra bring us information on the concentrations of Fe and Cr at different depths from the surface. The investigated Fe/Cr double layer and Fe-Cr alloys are known to have polycrystalline structure containing grain boundaries and compound intermixing and diffusion around Fe/Cr interface and oxygen diffusion into the layers [62] which can complicate the investigation of Cr segregation and interpretation of the results. AES together with XPS was used to carry out preliminary diffusion and depth profile experiments. AES depth profiles that were measured from untreated and heated Fe/Cr/Si layer samples are presented in Fig. 11. Annealing was performed in XPS located in the same room as AES but missing the possibility to transfer the sample in UHV between the spectrometers. XPS spectra were measured before and after every heating period (Fig. 11)

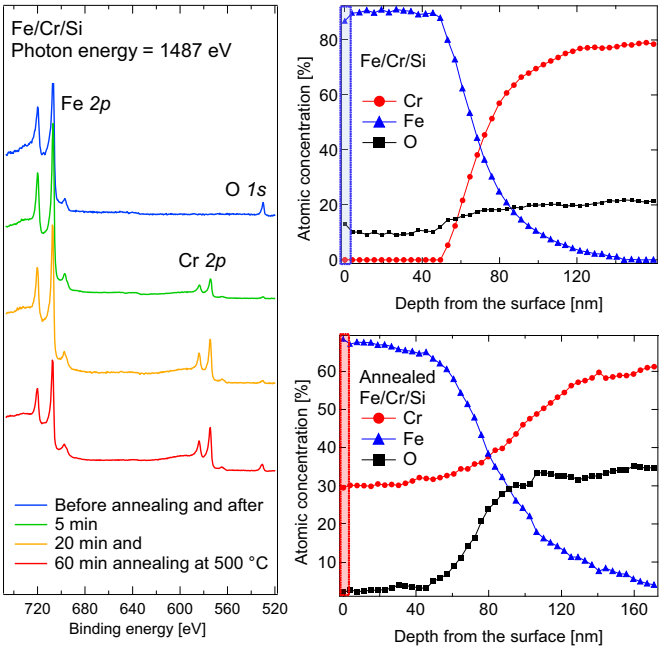

FIG. 11. (Color online) Left-hand side presents the Fe $2p$, Cr $2p$, and O $1s$ XPS spectra of a Fe/Cr bilayer sample before (topmost spectrum) and after annealing. These spectra were measured using Al Kα twin anode. Photoemission spectra clearly demonstrate the increase of Cr $2p$ intensity as a function of annealing time confirming the Cr diffusion into the Fe layer. The upper AES profile on the right is taken over the Fe/Cr interface before any heating was carried out starting sputtering from the surface represented by the uppermost XPS spectrum (blue) on the left. The lower AES depth profile on the right was taken after all the heating treatments starting from the surface concentration presented in the lowest (red) XPS spectrum on the left.

which were carried out at 500 °C for 5, 15, and 40 minutes giving a total heating time of 60 minutes. The pressure of the preparation chamber where the heating was performed was 3×10^{-8} Torr at maximum. The sample was cooled close to room temperature before measuring the spectra. The annealed sample was transferred to AES through air and two minutes of sputtering was performed before starting the depth profiling to get rid of the carbon contamination. The upper depth profile in Fig. 11 nicely presents the well separated Fe and Cr layers. It must be noted that the signal in the topmost XPS spectra at the same binding energy at which Cr $2s$ would appear (around 696 eV) is entirely due to the nonmonochromatic radiation used in laboratory XPS. About 10% oxygen concentration in the Fe layer is comparable to the topmost XPS spectrum in Fig. 11. The content of oxygen through the whole sample is quite high but can be explained by the fact that no protecting passive layer was formed on the surface of the Fe layer. Polycrystalline samples contain a number of grain boundaries or dislocations which can enhance the oxygen diffusion or diffusional transport of Cr towards the surface [64]. Also the pressure during the sample growth and sputtering with Ar^+ ions can have an effect on the oxygen concentration within the layers. The oxygen content increases in phase with Cr content in both profiles which in addition to the above-mentioned reasons is related to higher affinity of Cr for oxygen and Cr

reacting with inward diffused oxygen [65–67]. After heating the Fe/Cr bilayer for 60 min at 500 °C the layered structure has been destroyed and the Cr concentration within the first 40 nm is about 30% increasing after that up to 60% before any signal from the Si substrate was observed. The oxygen concentration for the annealed sample is less than 5% until fast decrease in Fe and slow increase of Cr concentration takes place at approximately the same depth from the surface where the original Fe/Cr interface was detected before heating. Oxygen concentration increases about the same percentage value as Cr concentration but more rapidly. This is expected since the diffusivity of O in bcc Fe [68] is much higher than diffusivity of Cr in Fe [69]. Most probably the reason for low oxygen concentration within the first 40 nm in the annealed double layer sample is due to the formation of a protective passive layer on the surface because of increased Cr concentration. The concentration at the uppermost atom layers of the annealed sample is not visible in Fig. 11 since some sputtering was done prior to the presented data to remove the contamination (carbon) that was absorbed on the surface during the sample transfer from XPS to AES.

To investigate the Cr segregation and also precipitation in Fe-Cr systems and to test our theoretical predictions the HAXPES technique was used to monitor the concentration profiles of the Fe/Cr double layer and chemical state of Fe and Cr atoms in two Fe-Cr alloys as a function of photon energy and heating time. Investigations were performed with photon energies from 2300 to 7300 eV in order to study the concentration profiles of the chemical components as a function of the probing depth. Prior to HAXPES experiments several annealing tests were performed with laboratory XPS to find the right annealing temperatures and time. The ideal temperature for Cr segregation in Fe/Cr/Si turned out to be 500 °C. At this temperature Cr diffused towards the surface in a few minutes time so that we were able to detect it with XPS. In the proper HAXPES segregation experiments the bilayer sample was heated in several steps as described above to gradually follow the Cr diffusion into the Fe layer (Fig. 12). Before starting the HAXPES segregation study the Fe layers of Fe/Cr/Si were cleaned in the UHV of the

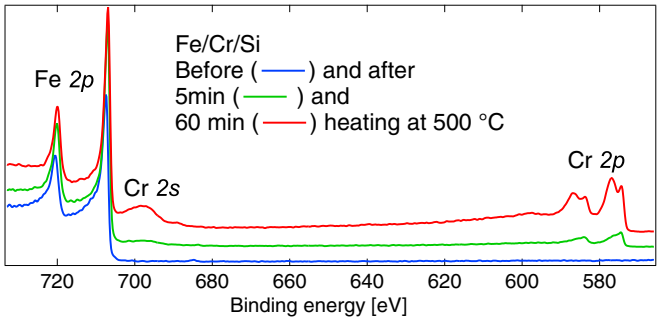

FIG. 12. (Color online) Overview HAXPES spectra of the Fe/Cr bilayer sample measured with 2300 eV photon energy before and after two heating treatments. In addition to the Cr 2s and Cr 2p spectra appearing after annealing, the increased intensity of Cr 2p as a comparison to Fe 2p after different annealing times demonstrates the Cr diffusion towards the surface. The intensity of Fe $2p_{3/2}$ of the presented spectra is normalized to 1 after setting background to zero.

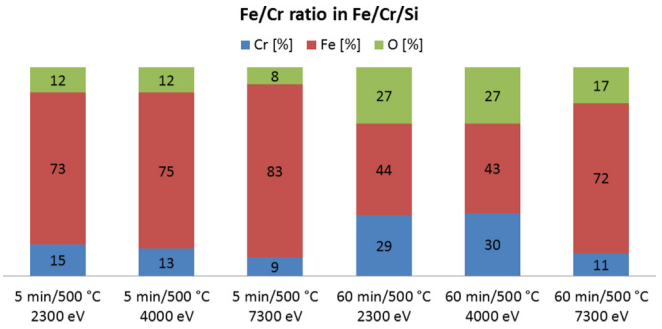

FIG. 13. (Color online) Concentrations of Cr, Fe, and O in Fe/Cr/Si. Relative intensities are calculated by analyzing the area of Cr 2p, Fe 2p, and O 1s spectra.

analyzer chamber of the HIKE spectrometer by annealing at 150 °C followed by 20 min Ar^+ sputtering. To start the Cr segregation investigations the quality of the Fe/Cr double layer structure, i.e., the absence of Cr in the Fe layer, was checked by scanning the binding energy range of Cr 2p and Cr 1s core levels before any heating was performed. Initially no Cr was found using 2300 eV, 4000 eV, and 7300 eV photon energies, i.e., experimental conditions that correspond to IMFP (λ) values from 2 to 7 nm and thus sampling depths (3λ) of approximately 9–20 nm depending on the oxidation and core-level studied [70,71]. It is worth mentioning that no Si was found in the spectra, either. This indicates the proper double layer structure of the sample: complete Fe layer on top of a Cr layer. Due to sputtering the thickness of the Fe layer before any heating treatments was less than in the AES studies being still more than 20 nm. After the cleaning procedure the sample was heated to 500 °C sequentially for 5, 15, and 40 minutes, total heating time being 5, 20, and 60 minutes, respectively. The spectra were measured after each heating period when the sample was cooled close to room temperature. The gradual changes of the atomic concentration profiles were observed with heating time (Fig. 12). These spectra nicely demonstrate the appearance of Cr spectra for heated samples. Before heating no signal at Cr 2p binding energy was observed but already after 5 min heating Cr 2s and Cr 2p signals appeared as shown in Fig. 12. The cross sections or spectrometer transmission are not taken into account in Fig. 12, which slightly underestimates the real intensity of Cr 2p and 2s photoemission signals relative to that of Fe 2p. The bulk concentrations of O, Cr, and Fe after short and longer heat treatments are shown in Fig. 13. Intensities presented in Fig. 13 are calculated by comparing the area of O 1s, Fe 2p, and Cr 2p spectra where Scofield cross sections [72], spectrometer transmission, and other experimental parameters have been taken into account. The Cr concentrations presented in Fig. 13 are in line with the AES depth profile in Fig. 11. The oxygen concentration for the heated sample derived from the HAXPES spectra is higher than the AES profiles give but this is most probably due to the pressure difference during the heating and measurements. Measurement with 2300 eV photon energy gives the average Cr concentration within 5 or 6 nm thick layer to be close to 15 at. % (Fig. 13). The concentrations in the 4000 eV photon energy measurements are similar but when compared to the more bulk-sensitive, 7300 eV photon

energy case, the Cr concentration is much lower than the Fe concentration. The increasing Cr concentration in the direction from bulk to the surface within the Fe layer of the heated sample is in line with our earlier calculations [14,15]. In $Fe_{0.95}Cr_{0.05}$ and $Fe_{0.85}Cr_{0.15}$ alloys the Cr segregation was not so evident. In the bulk (comparison of Fe $2p$ and Cr $2p$ spectra) almost no change in the Fe/Cr intensity ratio was detected but more surface-sensitive measurements of Cr and Fe $1s$ photoelectrons show some increase in Cr intensity as a result of heating, especially in the oxidized Cr.

3. *Oxidation*

Even after 5 min annealing at 500 °C at pressure of about 5×10^{-8} Torr the Fe/Cr bilayer sample and Fe-Cr alloys were evidently oxidized enabling the investigation of the ratio of alloy Cr and oxidized Cr. Oxidized Cr is well resolved on the high binding energy side of the alloy Cr (Fig. 14). A higher amount of oxidized Cr in the Fe/Cr bilayer was observed in the more surface-sensitive (photon energy = 2300 eV) Cr $2p$ HAXPES experiment [Fig. 14(a)] compared to the 4000 eV or 7300 eV measurements [73] indicating increasing Cr concentration towards the open surface also in the initial oxidation experiments, which is in line with our *ab initio* calculations on Fe-Cr alloy surface (Fig. 1) and on the Fe-Cr/Cr_2O_3 interface [15]. The spectra show also that, especially at room temperature range, oxygen penetration deeper into the metal is slow.

Figure 14 presents Cr $2p$ photoemission spectra of the bilayer sample after 5 and 60 minutes heating at 500 °C measured with 2300 eV photon energy (a) together with Cr $2p$ spectra of $Fe_{0.95}Cr_{0.05}$ and $Fe_{0.85}Cr_{0.15}$ alloys before and after heating 10 minutes at 500 °C [panels (b) and (c), respectively]. The spectra that were measured after 5 min annealing of Fe/Cr/Si (a) and before annealing of alloys [(b), (c)] present a fit with three components. The two components, Cr and Cr alloy, can be resolved due to the chemical shift between Cr atom surrounded mostly by other Cr atoms or Fe atoms. Thus segregation of Cr and formation of Cr dominating areas can be estimated by analyzing the fitted spectra. The broad feature from approximately 575 to 580 eV in all the spectra is the spectrum of the measured Cr_2O_3 reference sample detected with the same parameters as the actual samples. The appearance of this pronounced feature on the high binding energy side of the bulk and alloy Cr makes it possible to distinguish the oxidized Cr from the unoxidized one.

In Cr oxides the interaction between valence band $3d$ electrons and $2p$ vacancy core levels can create a number of final states which is called multiplet splitting [74,75]. For example, Biesinger *et al.* [74] have presented a fit for asymmetric Cr $2p$ photoemission spectra of Cr(III) oxide that consists of five components. In this study we have used the Cr_2O_3 reference spectrum to replace the multiple feature fit that otherwise would have been needed to properly describe the complicated multiplet splitting of Cr(III) oxide [74]. However, the Cr $2p$ photoemission spectra cannot be fitted satisfactorily by using only the Cr_2O_3 reference spectrum and one asymmetric Voigt-line-shaped feature to describe the unoxidized Fe-Cr alloy. An additional component is needed between Cr_2O_3 and Cr alloy features. This structure

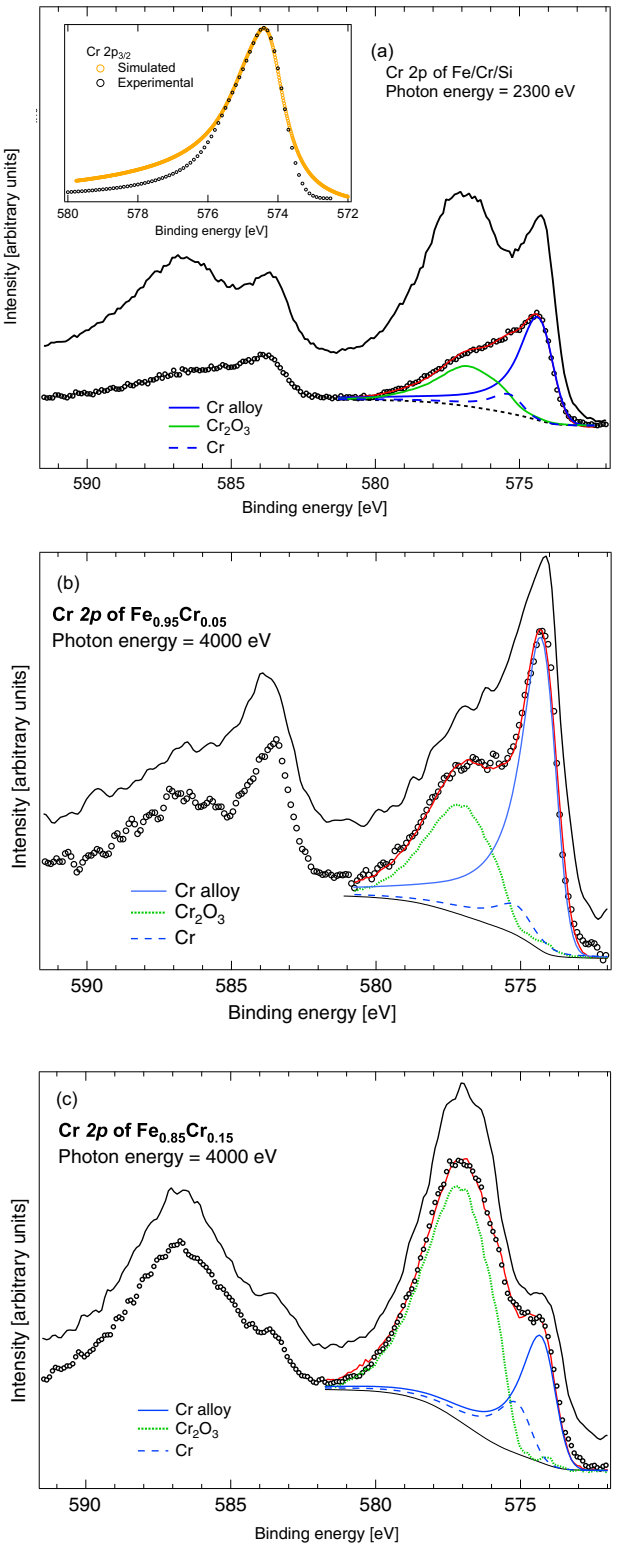

FIG. 14. (Color online) Cr $2p$ spectra of Fe/Cr bilayer sample after 5 (open circles) and 60 min (solid line) heating (a) and Cr $2p$ spectra of $Fe_{0.95}Cr_{0.05}$ (b) and $Fe_{0.85}Cr_{0.15}$ (c) alloys before and after heating 10 minutes at 500 °C. The lower spectra in (a), (b), and (c) are fitted using three components to represent signals from bulklike Cr, Cr from Fe-Cr alloy, and oxidized Cr. The simulated Cr $2p_{3/2}$ line shape for the Fe/Cr/Si sample at 2300 eV photon energy after 5 min heating is compared to the experimental spectrum which is a sum of Cr and Cr alloy components [inset of (a)].

at approximately 575.4 eV binding energy originates from bulklike chromium (Cr-Cr) (labeled Cr in Fig. 14). The shift between the Cr alloy and Cr components in the fitted spectra is approximately 0.9–1 eV, which is close to the value we observed in our HAXPES measurements of pure, unoxidized Cr and Cr_2O_3 reference samples. The asymmetry parameter and full width at half maximum (FWHM) value used for Cr and Cr alloy line shape in the fitting procedure were derived from the HAXPES spectra of the Cr bulk reference. In addition to the experimental arguments, first-principles calculations within density functional theory using the complete screening picture [76] were performed to estimate the binding energy shift between bulk Cr and $Fe_{1-x}Cr_x$ alloys of different concentrations. These calculations gave a negative binding energy shift for Cr $2p$ core level spectra which was between -0.1 and -0.5 eV for Cr concentrations $x = 0.1$–0.9 being largest in the case of $Fe_{0.8}Cr_{0.2}$.

The calculated *ab initio* Cr $2p_{3/2}$ core level shifts were used to simulate the 2300 eV line shape of the alloy section of the Cr $2p_{3/2}$ spectrum of Fe/Cr/Si. At first a model for Cr concentration was set up. The concentration is assumed to be homogeneous in the direction parallel to the surface plane, and perpendicular to it to have a parametrized form $c_{Cr}(d)$, where d is the distance from the surface. This trial function consists of two constant sections describing the Cr-segregated surface region and the bulk part. These two sections of the trial function are joined together with a linear slope. Thus, the function $c_{Cr}(d)$ contains four parameters: the width (w_s) and height (h_s) in the surface region, the height (h_b) in the bulk part, and the width (w_j) of the linear slope. Then the parameters of the trial function were determined by fitting to the ratios of the experimental intensities shown in Fig. 13. The parameter h_s was taken to be 1 (assuming pure Cr layer on the surface) and the optimized values are ($h_b = 0.09$, $w_s = 0.5$ nm, $w_j = 1$ nm) for the 5 min annealed sample and ($h_b = 0.03$, $w_s = 3$ nm, $w_j = 1$ nm) for the 60 min annealed sample. The total line shape of the Cr $2p_{3/2}$ spectrum is then obtained by discretizing the sample into thin films parallel to the surface and summing up the partial line shapes of Cr $2p_{3/2}$ related to these films. Before summation each partial line shape is shifted by the calculated concentration-dependent core level shift, broadened with 1.3 eV by the Doniach-Sunjic procedure, and multiplied by the weight factor (product of the local Cr concentration and the exponential damping according to IMFP λ). The obtained Cr $2p_{3/2}$ line shape, compared with the experimental one (sum of fitted Cr and Cr alloy components), is shown in the inset in Fig. 14(a).

Even though the samples were measured in ultrahigh vacuum the Cr oxidation was evident. However, almost no sign of Fe oxide was seen in the Fe photoemission spectra. As presented already in Fig. 14 the intensity of Cr in Fe/Cr/Si further increased between the 5 and 60 minutes heating and in the latter spectrum a larger number of Cr atoms is detected as an oxide than in metallic form [Fig. 14(a)]. During the 60 min annealing the amount of Fe decreases (Fig. 13) to a lower level due to Cr segregation [Fig. 14(a)] and the oxidized form of Fe is not resolved even on the surface. As a comparison to the unoxidized (sputtered until no traces of O or C were detected) bulk Fe reference sample only the surface-sensitive Fe $1s$ spectrum of Fe/Cr/Si (not shown here) that was measured before any heating shows slightly increased intensity on the high binding energy side where oxidized Fe would show.

The Cr $2p$ spectra of $Fe_{0.95}Cr_{0.05}$ and $Fe_{0.85}Cr_{0.15}$ alloys in Figs. 14(b) and 14(c) show how the concentration can affect the formation of the oxide layer already at very low pressure (10^{-8} Torr). These spectra were measured using 4 keV photon energy in which case the share of the surface layer (topmost 5 nm) has here a smaller role than in the Fe/Cr/Si spectra of Fig. 14(a). In the case of higher Cr bulk concentration alloy ($Fe_{0.85}Cr_{0.15}$) most of the Cr atoms are oxidized even before any heating was carried out. The fraction of the Cr_2O_3 component of the total Cr $2p_{3/2}$ signal area is 55% for $Fe_{0.85}Cr_{0.15}$ and 23% for $Fe_{0.95}Cr_{0.05}$ alloy. The $Fe_{0.85}Cr_{0.15}$ alloy having more oxide on the surface than the $Fe_{0.95}Cr_{0.05}$ alloy is in line with our *ab initio* predictions that the pristine surface of $Fe_{0.85}Cr_{0.15}$ alloy should contain more chromium than the pristine surface of $Fe_{0.95}Cr_{0.05}$ alloy; i.e., there is more chromium to be oxidized on the surface of $Fe_{0.85}Cr_{0.15}$ compared to the surface of $Fe_{0.95}Cr_{0.05}$. In $Fe_{0.95}Cr_{0.05}$ the heating seems to remove part of the Cr_2O_3 relative to unoxidized Cr making the Cr/Cr oxide signal ratio slightly increase. Still the amount of unoxidized Cr stays approximately the same despite the heating. Also here only the Cr atoms were oxidized.

4. Cr solubility and precipitation

While the total amount of Cr increases considerably in Fe/Cr/Si (Fig. 13) due to additional heating the share of oxidized Cr has the highest proportion. On the other hand, the Fe $2p$ spectra measured with photon energy of 7300 eV reveal that with heating the Fe concentration in the bulk part of the Fe-layer changes only moderately compared to the surface region (Fig. 13), implying similarly moderate changes for the Cr content in the bulk part of the Fe layer. As the MCMD simulations show, in the Fe/Cr double layer system chromium is dissolved in the iron layer up to the Cr solubility limit: 6 at. % at 300 K and 12 at. % at 700 K (Fig. 8). Thus our MCMD result for the Cr solubility limit is in line with the present HAXPES measurements of the 5 and 60 minutes annealed Fe/Cr double layer showing that the Cr concentration is lowest in the Fe film between the underlying Cr layer and the surface region. This demonstrates the existence of the upper limit for the Cr solubility in Fe in line with our *ab initio* (Table I) and semiempirical (Fig. 9) calculations. In the investigated case the Fe layer acts as a retarder for the Cr diffusion from the deeper lying Cr reservoir towards the surface and the Cr enrichment to the surface.

The MCMD simulations of formation of Cr-rich α' precipitates at different temperatures with different Cr concentration in $Fe_{1-x}Cr_x$ systems are presented in Fig. 6. The experimental techniques used in this study are not suitable to study precipitation in such a resolution that the measurements could be carried out only for the areas where precipitates occur as a comparison to the alloy areas. However, the binding energy of Cr atoms is very sensitive to their chemical state which is why a combination of the Cr bulk reference sample spectra and information based on first-principles calculations using the complete screening picture was used to fit the Cr $2p$ spectra (Fig. 14). The feature labeled Cr has higher binding energy than the component that describes the fraction of Cr atoms in

Fe-Cr alloy. This difference depends on the Cr concentration in alloy being here approximately 0.9 eV referring to a Cr concentration around 15–30 at. % which causes the largest negative binding energy shift as a comparison to 100% Cr. The feature labeled Cr originates from atoms that have more other Cr atoms than Fe (or O) atoms as nearest neighbors. In alloys where Cr concentration is as low as 5 or 15 at. % the origin of this Cr bulklike structure can be either formation of a Cr-rich layer under the topmost surface atom layers due to segregation or precipitation of Cr. Cr can also have a high concentration on the grain boundaries but then it would most likely be oxidized. According to the simulations in alloys with Cr bulk concentration exceeding 10 at. % (Fig. 6) Cr-rich α' precipitates can be found already at room temperature. In the experiments the relative intensity (area of the Cr component) increases considerably from $Fe_{0.95}Cr_{0.05}$ to $Fe_{0.85}Cr_{0.15}$ alloy being approximately 7% and 12%, respectively. This trend suggests that at least part of the Cr signal can be caused by the Cr-segregated α' phase, i.e., Cr precipitates in bulk, being in line with the theory.

However, more detailed experiments and discussion of the bilayer sample and Fe-Cr alloys are still needed before more thorough conclusions about precipitation and oxidation states of Cr after every heating step can be drawn. Here the fit is used to give a better picture of how the method can be used to follow the rate of oxidation and progression of Cr segregation and to estimate the Cr concentration over the analyzed sample layer. When comparing the AES, XPS, and HAXPES results besides resolution and probing depth of the techniques, it is essential to keep in mind the possible effect of sputtering on the chemical composition of the bilayers, the different rate of oxidation caused by differences in analyzer chamber pressures, and possible treatment and transfer of the samples prior to the measurements. All these mentioned parameters were set to meet each other as well as possible and the differences have been taken into account when analyzing the results.

To summarize the experimental findings, Cr diffusion to the Fe layer in the Fe/Cr double layer sample was investigated by depth profiling. The formation of Cr-rich layers or precipitates in the Fe/Cr double layer and in Fe-Cr alloys was investigated by analyzing the chemical shift of Cr $2p$ core-level spectra. Initial oxidation took place already at high vacuum circumstances which was verified by formation of Cr_2O_3. Calculations and simulations are performed for single crystals as all the measurements were done for polycrystalline samples which were also oxidized. This evidently makes the comparison between the results more complicated. However, the experimental results of Cr solubility in Fe, intermixing of the Fe/Cr interface, Cr diffusion to Fe, and formation of Cr-rich areas in Fe-Cr alloys are in line with the theory.

IV. CONCLUSIONS

Due to the major challenges related to the investigation of long-range properties of materials as a function of different internal and external parameters we have used in the present investigation a multiscale and interdisciplinary approach. The EMTO method has been used to investigate atomic-scale properties, the MCMD method is applied for exploring the large-scale bulk phenomena, and several spectroscopic techniques have been used to study properties related to kinetics and oxidation.

The *ab initio* EMTO calculations predict that in the initially homogeneous $Fe_{1-x}Cr_x$ the net driving force of the migration of Cr atoms is from the second atomic layer to the bulk for low-Cr alloys ($c_{Cr} \lesssim 10$ at. %) and to the surface for moderate-Cr alloys ($c_{Cr} \gtrsim 10$ at. %). Comparing the bulk and surface the calculations predict the driving force to be from the surface to the bulk ($c_{Cr} \lesssim 10$ at. %) and from the bulk to the surface ($c_{Cr} \gtrsim 10$ at. %); i.e., the *ab initio* simulations predict Cr-containing surfaces when Cr concentration exceeds $\sim$10 at. %.

For Cr concentration regions less than 10 at. %, the *ab initio* CPA-EMTO result of the important role of the second atomic layer to the surface is not reproducible from the large-scale MCMD simulation. Instead, for the regions of the nominal concentration larger than 10 at. % Cr the MCMD simulations predict the formation of Cr-rich precipitates. Increasing the Cr concentration the excess chromium goes to the precipitates. Due to the Cr surface and segregation energies the precipitates do not reach the surface layer and, consequently, there is no large thermodynamic driving force to push Cr atoms to the surface. In ambient conditions oxidation of Cr changes the picture. Surface Cr is oxidized and the oxide-alloy interface forms a sink to the Cr of the alloy phase. One should, however, note that these simulations only give the thermodynamic equilibrium states. Kinetics of the alloy microstructure and surface oxidation can be expected to have an effect on the surface structure. Simulations of Fe/Cr layer structure show the temperature-dependent upper limit of the solubility of Cr in Fe $\sim$ 6 at. % at 300 K and $\sim$12 at. % at 700 K.

Experimental investigations concentrated on Cr segregation and precipitation together with initial oxidation of Fe-Cr systems. Both AES and HAXPES measurements support the MCMD simulations for high Cr concentration alloys. The segregation of Cr was nicely demonstrated in the spectra by annealing the Fe/Cr double layer and following the diffusion of Cr towards the surface. This was done using both AES and HAXPES measurements. Besides comparison of the intensity of Cr and Fe core level spectra in the Fe/Cr double layer and Fe-Cr alloys, more detailed information on the chemical state of Cr atoms was derived from the deconvoluted Cr $2p$ spectra. The fitting procedure suggested that some of the Cr atoms have bulk-Cr-like structure which can be connected to the formation of Cr-rich precipitates where the nearest neighbors of Cr atoms are other Cr atoms instead of Fe (or O) atoms. The share of this Cr signal was much higher for $Fe_{0.85}Cr_{0.15}$ than for $Fe_{0.95}Cr_{0.05}$ alloy which is in line with the MCMD simulations. Initial oxidation of Fe-Cr systems is provably very demanding to investigate because of very fast Cr oxide formation in freshly cleaned samples even at very low pressure, in the UHV of the analyzer chamber of spectrometers. Cr was the only compound that was oxidized during and after annealing and the formation of Cr_2O_3 was verified by using the reference spectra and fitting procedure.

In order to further improve the understanding of the properties and phenomena related to Fe-Cr in different ambient conditions, the development of trends such as MC simulations using potentials which properly take account of the surface effects (e.g., enhanced magnetic moments), as well as more extensive DFT simulations using effective chemical potentials

in kinetics, would be advantageous. The developing HAXPES technique will also provide more selective research methods in the future.

ACKNOWLEDGMENTS

We thank HZB for the allocation of synchrotron radiation beamtime and Dr. Mihaela Gorgoi for all the guidance and help during the experiments. The research leading to these results has received funding from the European Community's Seventh Framework Programme (FP7/2007-2013) under Grant Agreement No. 312284. Academy of Finland (Grant 132428) is greatly acknowledged by SG. Dr. Giovanni Bonny is acknowledged for providing the 2BEAM data for the authors' use. The computational facilities provided by the IT Centre for Science, Espoo, Finland, and the Finnish Grid Infrastructure project are gratefully acknowledged.

[1] L. Vitos, H. L. Zhang, S. Lu, N. Al-Zoubi, B. Johansson, E. Nurmi, M. Ropo, M. Punkkinen, and K. Kokko, *Alloy Steel: Properties and Use* (INTECH, 2011).
[2] Y. Weng, H. Dong, and Y. Gan, eds., *Advanced Steels: The Recent Scenario in Steel Science and Technology* (Springer-Verlag, 2011).
[3] S. K. Burke, R. Cywinski, J. R. Davis, and B. D. Rainford, J. Phys. F: Met. Phys. **13**, 451 (1983).
[4] P. Grunberg, R. Schreiber, Y. Pang, M. B. Brodsky, and H. Sowers, Phys. Rev. Lett. **57**, 2442 (1986).
[5] F. Danoix and P. Auger, Mater. Charact. **44**, 177 (2000).
[6] J. Cieślak, S. M. Dubiel, and B. Sepiol, J. Phys.: Condens. Matter **12**, 6709 (2000).
[7] G. Bonny, D. Terentyev, and L. Marelba, Scr. Mater. **59**, 1193 (2008).
[8] S. Novy, P. Pareige, and C. Pareige, J. Nucl. Mater. **384**, 96 (2009).
[9] C. Pareige, M. Roussel, S. Novy, V. Kuksenko, P. Olsson, C. Domain, and P. Pareige, Acta Mater. **59**, 2404 (2011).
[10] G. Riedrich and F. Loib, Archiv für das Eisenhüttenwesen **15**, 175 (1941).
[11] J. K. Sahu, U. Krupp, R. N. Ghosh, and H.-J. Christ, Mater. Sci. Eng. A **508**, 1 (2009).
[12] M. Levesque, Phys. Rev. B **87**, 075409 (2013).
[13] G. Wranglén, *An Introduction to Corrosion and Protection of Metals* (Chapman and Hall, New York, 1985).
[14] M. Ropo, K. Kokko, M. P. J. Punkkinen, S. Hogmark, J. Kollár, B. Johansson, and L. Vitos, Phys. Rev. B **76**, 220401 (2007).
[15] M. P. J. Punkkinen, K. Kokko, H. Levämäki, M. Ropo, S. Lu, L. Delczeg, H. L. Zhang, E. K. Delczeg-Czirjak, B. Johansson, and L. Vitos, J. Phys.: Condens. Matter **25**, 495501 (2013).
[16] W. T. Geng, Phys. Rev. B **68**, 233402 (2003).
[17] G. J. Ackland, Phys. Rev. Lett. **97**, 015502 (2006).
[18] A. V. Ponomareva, E. I. Isaev, N. V. Skorodumova, Y. K. Vekilov, and I. A. Abrikosov, Phys. Rev. B **75**, 245406 (2007).
[19] A. Kiejna and E. Wachowicz, Phys. Rev. B **78**, 113403 (2008).
[20] G. J. Ackland, Phys. Rev. B **79**, 094202 (2009).
[21] M. Levesque, M. Gupta, and R. P. Gupta, Phys. Rev. B **85**, 064111 (2012).
[22] P. Hohenberg and W. Kohn, Phys. Rev. **136**, B864 (1964).
[23] W. Kohn and L. J. Sham, Phys. Rev. **140**, A1133 (1965).
[24] L. Vitos, I. A. Abrikosov, and B. Johansson, Phys. Rev. Lett. **87**, 156401 (2001).
[25] L. Vitos, *Computational Quantum Mechanics for Materials Engineers: The EMTO Method and Applications* (Springer-Verlag, London, 2007).
[26] J. P. Perdew, K. Burke, and M. Ernzerhof, Phys. Rev. Lett. **77**, 3865 (1996).
[27] L. Vitos, Phys. Rev. B **64**, 014107 (2001).
[28] P. Soven, Phys. Rev. **156**, 809 (1967).
[29] M. Ropo, K. Kokko, E. Airiskallio, M. P. J. Punkkinen, S. Hogmark, B. J. J. Kollár, and L. Vitos, J. Phys.: Condens. Matter **23**, 265004 (2011).
[30] M. Ropo, K. Kokko, L. Vitos, J. Kollár, and B. Johansson, Surf. Sci. **600**, 904 (2006).
[31] P. Olsson, I. A. Abrikosov, and J. Wallenius, Phys. Rev. B **73**, 104416 (2006).
[32] G. Bonny, D. Terentyev, and L. Malerba, Comput. Mater. Sci. **42**, 107 (2008).
[33] G. Bonny, R. C. Pasianot, D. Terentyev, and L. Malerba, Philos. Mag. **91**, 1724 (2011).
[34] M. Y. Lavrentiev, R. Drautz, D. Nguyen-Manh, T. P. C. Klaver, and S. L. Dudarev, Phys. Rev. B **75**, 014208 (2007).
[35] M. Levesque, E. Martínez, C.-C. Fu, M. Nastar, and F. Soisson, Phys. Rev. B **84**, 184205 (2011).
[36] E. Martínez, O. Senninger, C. C. Fu, and F. Soisson, Phys. Rev. B **86**, 224109 (2012); E. Martínez, C.-C. Fu, M. Levesque, M. Nastar, and F. Soisson, Solid State Phenom. **172–174**, 1016 (2011).
[37] O. Senninger, E. Martínez, F. Soisson, M. Nastar, and Y. Bréchet, Acta Mater. **73**, 97 (2014).
[38] P. Erhart, A. Caro, M. Serrano De Caro, and B. Sadigh, Phys. Rev. B **77**, 134206 (2008).
[39] D. Terentyev, X. He, E. Zhurkin, and A. Bakaev, J. Nucl. Mater. **408**, 161 (2011).
[40] E. E. Zhurkin, D. Terentyev, M. Hou, L. Malerba, and G. Bonny, J. Nucl. Mater. **417**, 1082 (2011).
[41] J. Wallenius, P. Olsson, C. Lagerstedt, N. Sandberg, R. Chakarova, and V. Pontikis, Phys. Rev. B **69**, 094103 (2004).
[42] G. Bonny, D. Terentyev, L. Malerba, and D. Van Neck, Phys. Rev. B **79**, 104207 (2009).
[43] G. Bonny, D. Terentyev, and L. Malerba, J. Nucl. Mater. **385**, 278 (2009).
[44] C. Pareige, C. Domain, and P. Olsson, J. Appl. Phys. **106**, 104906 (2009).
[45] N. Castin and L. Malerba, J. Chem. Phys. **132**, 074507 (2010).
[46] N. Castin, G. Bonny, D. Terentyev, M. Lavrentiev, and D. Nguyen-Manh, J. Nucl. Mater. **417**, 1086 (2011).
[47] D. Terentyev, N. Castin, and C. J. Ortiz, J. Phys.: Condens. Matter **24**, 475404 (2012).

[48] P. Olsson, J. Wallenius, C. Domain, K. Nordlund, and L. Malerba, Phys. Rev. B **72**, 214119 (2005).
[49] M. Gorgoi, S. Svensson, F. Schaefers, G. Ohrwall, M. Mertin, P. Bressler, O. Karis, H. Siegbahn, A. Sandell, H. Rensmo, W. Doherty, C. Jung, W. Braun, and W. Eberhardt, Nucl. Instrum. Methods Phys. Res. **601**, 48 (2009).
[50] T. P. C. Klaver, R. Drautz, and M. W. Finnis, Phys. Rev. B **74**, 094435 (2006).
[51] D. Nguyen-Manh, M. Y. Lavrentiev, and S. L. Dudarev, J. Comput.-Aided Mater. Des. **14**, 159 (2007).
[52] D. Nguyen-Manh, M. Y. Lavrentiev, and S. L. Dudarev, C. R. Phys. **9**, 379 (2008).
[53] D. Nguyen-Manh and S. L. Dudarev, Phys. Rev. B **80**, 104440 (2009).
[54] M. Y. Lavrentiev, D. Nguyen-Manh, and S. L. Dudarev, Phys. Rev. B **81**, 184202 (2010).
[55] M. Y. Lavrentiev, R. Soulairol, C.-C. Fu, D. Nguyen-Manh, and S. L. Dudarev, Phys. Rev. B **84**, 144203 (2011).
[56] C.-C. Fu, M. Y. Lavrentiev, R. Soulairol, S. L. Dudarev, and D. Nguyen-Manh, Phys. Rev. B **91**, 094430 (2015).
[57] M. Sladecek, B. Sepiol, M. Kaisermayr, B. H. J. Korecki, H. Thiess, O. Leupold, R. Ruffer, and G. Vogl, Surf. Sci. **507–510**, 124 (2002).
[58] M. Punkkinen, Q.-M. Hu, S. Kwon, B. Johansson, J. Kollár, and L. Vitos, Philos. Mag. **91**, 3627 (2011).
[59] M. P. J. Punkkinen, S. K. Kwon, J. Kollár, B. Johansson, and L. Vitos, Phys. Rev. Lett. **106**, 057202 (2011).
[60] B.-Q. Fu, W. Liu, and Z.-L. Li, Appl. Surf. Sci. **255**, 8511 (2009).
[61] S. Lu, Q.-M. Hu, B. Johansson, and L. Vitos, Phys. Status Solidi B **248**, 2087 (2011).
[62] O. Fedchenko, S. Protsenko, P. Zukowski, and M. Marszalek, Vacuum **86**, 1934 (2012).
[63] CasaXPS Manual 2.3.15 Rev. 1.3, Casa Software Ltd., http://www.casaxps.com/ebooks/OrangeBookRev1.3ebook.pdf.
[64] C. Ostwald and H. J. Grabke, Corr. Sci. **46**, 1113 (2004).
[65] J. Camra, E. Bielanska, A. Bernasik, K. Kowalski, M. Zimovska, A. Bialas, and M. Najbar, Catal. Today **105**, 629 (2005).
[66] B. Pujilaksono, T. Jonsson, H. Heidari, M. Halvarsson, J. Svensson, and L. Johansson, Oxid. Met. **75**, 183 (2011).
[67] T. Horita, H. Kishimoto, K. Yamaji, Y. Xiong, M. E. Brito, H. Yokokawa, Y. Baba, K. Ogasawara, H. Kameda, Y. Matsuzaki, S. Yamashita, N. Yasuda, and T. Uehara, Solid State Ionics **179**, 2216 (2008).
[68] S. L. Shang, H. Z. Fang, J. Wang, C. P. Guo, Y. Wang, P. D. Jablonski, Y. Du, and Z. K. Liu, Corr. Sci. **83**, 94 (2014).
[69] K. Takasawa, Y. Yamazaki, S. Takaki, K. Abiko, and Y. Iijima, Mater. Trans. **43**, 178 (2002).
[70] S. Tanuma, C. J. Powell, and D. R. Penn, Surf. Interface Anal. **35**, 268 (2003).
[71] C.-O. A. Olsson, S. Malmgren, M. Gorgoi, and K. Edström, Electrochem. Solid-State Lett. **14**, C1 (2011).
[72] J. H. Scofield, Lawrence Livemore Laboratory Report **UCRL-51326**, 63 and 67 (1973).
[73] K. Kokko, S. Granroth, M. H. Heinonen, R. E. Perälä, T. Kilpi, E. Kukk, M. P. J. Punkkinen, E. Nurmi, M. Ropo, A. Kuronen, and L. Vitos, Mater. Sci. Forum **762**, 728 (2013).
[74] M. C. Biesinger, B. P. Payne, A. P. Grosvenor, L. W. M. Lau, A. R. Gerson, and R. S. C. Smart, Appl. Surf. Sci. **257**, 2717 (2011).
[75] R. P. Gupta and S. K. Sen, Phys. Rev. B **12**, 15 (1975).
[76] W. Olovsson, T. Marten, E. Holmstrm, B. Johansson, and I. A. Abrikosov, J. Electron. Spectrosc. Relat. Phenom. **178–179**, 88 (2010).